Physics Letters A 593 (2026) 132054

Contents lists available at ScienceDirect

Physics Letters A

journal homepage: www.elsevier.com/locate/pla

Letter

Quantifying magnetic moments with phase-based electron-optical nanomagnetometry

Hangbo Su [a], Xianhui Ye [a], Jiaqi Su [a], Yuying Liu [a], Zian Li [a,*], András Kovács [b], Rafal E. Dunin-Borkowski [b], Marco Beleggia [c]

[a] School of Physical Science and Technology, Guangxi University, Nanning, 530004, Guangxi, China
[b] Ernst Ruska-Centre for Microscopy and Spectroscopy with Electrons, Forschungszentrum Jülich GmbH, Jülich, 52425, Germany
[c] Department of Physics, University of Modena and Reggio Emilia, Modena, 41125, Italy

ARTICLE INFO

Communicated By Jia Grace Lu

Keywords:
Magnetic moment
Off-axis electron holography
Closed-path phase integration
Demagnetization factor
Magnetic nanoparticles

ABSTRACT

Quantifying the magnetic moment of individual nanostructures with high spatial resolution and accuracy remains a challenge. We establish a theoretical framework linking the electron-optical phase shift to the absolute magnetic moment and introduce a robust phase-integration method for its direct measurement. The approach is validated through simulation and experiment, enabling quantitative nanoscale magnetic analysis in the transmission electron microscope.

Measuring the fundamental electromagnetic properties of nanomaterials is essential for understanding their behavior in devices such as single-electron transistors and magnetic memory bits [1–9]. Yet doing so at the nanoscale is difficult: it requires both high spatial resolution and sensitivity to faint signals [10,11]. Transmission electron microscopy (TEM) has become a quantitative tool for electromagnetic field mapping [12–14], with electron holography as a central technique [15]. The measured phase shift $\varphi(x, y)$ is proportional to the projected electrostatic potential $V(x, y, z)$ and magnetic vector potential $\boldsymbol{A}(x, y, z)$ [16], encoding information about both electric field and magnetic induction within and around the sample.

Frameworks for extracting quantitative information about electric and magnetic fields from phase images are well established [17,18]. For electric charge q_e, the relationship is straightforward: the phase shift connects directly to the projected potential, allowing quantification at single-electron precision [19,20]. For magnetic moment $\mathbf{m}$, the situation is more complicated [21]. The link between the phase image and the magnetic vector potential involves the vector nature of the field and the influence of sample shape and magnetic microstructure [22]. This complexity can obscure the underlying physics, and the lack of intuitive understanding has kept these techniques from spreading beyond specialized groups [23,24].

We previously introduced a method to measure magnetic moments from electron-optical phase images by integrating the phase along a closed path encircling the particle [21,25,26]. The result is the inductive moment $\mathbf{m}^{\mathrm{B}}$, which is proportional to the out-of-plane component of the magnetic moment $\mathbf{m}_{x,y}$ through a constant that does not depend on the particle's shape, composition, or magnetic state [21]. This universality makes the method mathematically elegant and experimentally convenient. Yet despite its appeal, the method has not seen wide adoption. What has been lacking is an intuitive physical explanation for why integrating the phase around a loop yields the magnetic moment.

Here we revisit the theory behind phase integration, focusing on the physical ideas rather than the mathematical steps. We show that the constant linking the integrated phase to the magnetic moment is simply the demagnetization factor of the sample [27]. We present a full three-dimensional derivation of this relationship, examine error sources in electron holography–including terms beyond the quadratic phase error considered previously [21]–and suggest ways to correct for them. Finally, we demonstrate how to apply the framework to experimental phase images, connecting the theory to practical measurement.

We begin by establishing the relationship between the measured electron-optical phase shift and the magnetic induction of the sample. Fig. 1(a) shows the off-axis electron holography (OAEH) setup. A coherent electron wave splits into an object wave passing through the specimen and a reference wave traveling through vacuum. Their interference produces a hologram encoding the phase shift $\varphi(x, y)$ imparted by the sample. This phase shift is proportional to the line integral of the

* Corresponding author.
E-mail address: zianli@gxu.edu.cn (Z. Li).

https://doi.org/10.1016/j.physleta.2026.132054
Received 16 May 2026; Accepted 29 July 2026
Available online 3 August 2026

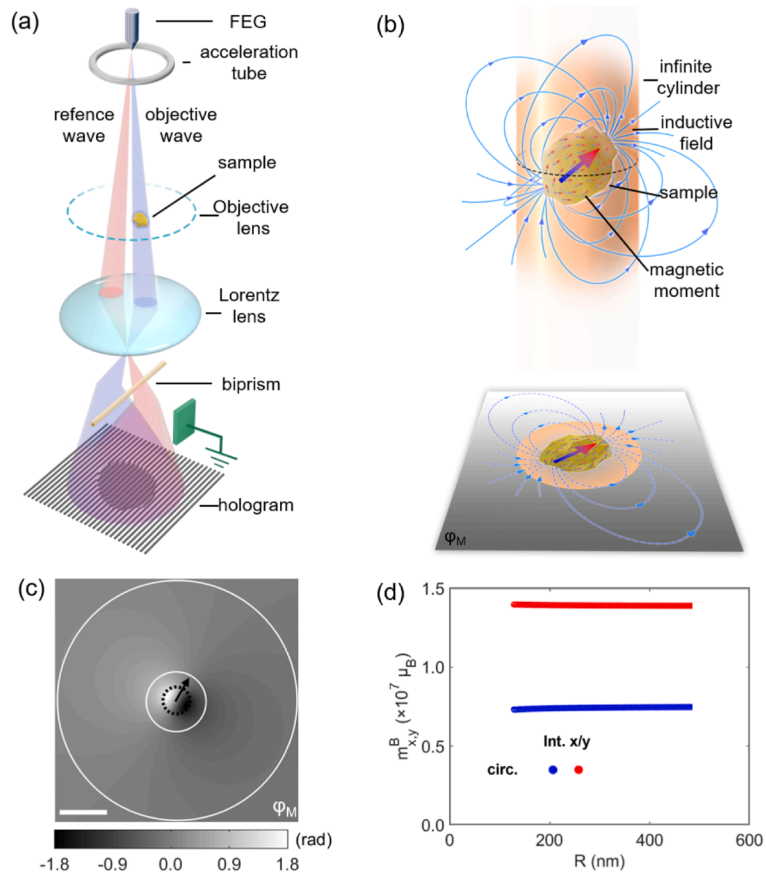

Fig. 1. Mapping magnetic induction via off-axis electron holography Mapping magnetic induction via off-axis electron holography (OAEH). (a) schematic of the experimental setup: interference between object and reference waves encodes the magnetic phase shift in a hologram. (b) principle of magnetic phase imaging: a magnetized nanoparticle imprints a phase shift φ_M on the transmitted electron wave. (c) simulated φ_M for a uniformly magnetized nanosphere (diameter 50 nm, $B_{xy} = 0.7$ T, magnetization tilted 61° from the x axis). Scale bar: 200 nm. (d) convergence of the total in-plane moment $\mathbf{m}_{xy}$ obtained from line integrals of φ_M along concentric circular paths with increasing radius.

electromagnetic potentials along the electron beam direction (z) [15]:

$$\varphi(x, y) = \frac{e}{\hbar v}\int_{-\infty}^{+\infty} V(x, y, z)\,\mathrm{d}z - \frac{e}{\hbar}\int_{-\infty}^{+\infty} A_z(x, y, z)\,\mathrm{d}z, \tag{1}$$

where e is the elementary charge, $\hbar$ the reduced Planck constant, and v the relativistic electron velocity. The first term arises from the electrostatic potential V, the second from the z-component of the magnetic vector potential $\mathbf{A}$.

For a non-uniform magnetic moment distribution, the total moment is $\bar{\mathbf{m}} = \sum_i \mathbf{m}_i$, equivalent to a single magnetic dipole (Fig. 1(b)) [28]. Outside the sample, the magnetic induction is the superposition of fields from each dipole.

We previously introduced a method to determine the magnetic moment of a nanoparticle from a phase image by integrating the phase over a circular path enclosing the structure [21]. Here we expand on this foundation with a rigorous exposition clarifying the physical interpretation and underlying assumptions.

The magnetic phase shift φ_M is given by

$$\varphi_M(\mathbf{r}_\perp) = -\frac{\pi}{\phi_0}\int_{-\infty}^{+\infty} A_z(\mathbf{r}_\perp, z)\mathrm{d}z, \tag{2}$$

where $\mathbf{r}_\perp = (x, y)$ and $\phi_0 = h/2e$ is the flux quantum. Taking the gradient yields the projected in-plane induction:

$$\mathbf{B}^{\mathrm{p}}(\mathbf{r}_\perp) = \frac{\phi_0}{\pi}[-\partial_y\varphi_M(\mathbf{r}_\perp),\ \partial_x\varphi_M(\mathbf{r}_\perp)]. \tag{3}$$

Integrating the phase gradient over a domain D gives

$$\frac{\phi_0}{\pi}\iint_D \nabla\varphi_M(\mathbf{r}_\perp)\mathrm{d}^2\mathbf{r}_\perp = \iiint_{D\otimes\mathbb{R}} [B_y(\mathbf{r}), -B_x(\mathbf{r})]\mathrm{d}^3\mathbf{r}, \tag{4}$$

where $D\otimes\mathbb{R}$ is the infinite cylinder with cross-section D along $\hat{\mathbf{z}}$. We define the *inductive moment*

$$\mathbf{m}^{\mathrm{B}} \equiv \frac{1}{\mu_0}\iiint_{D\otimes\mathbb{R}} \mathbf{B}(\mathbf{r})\mathrm{d}^3\mathbf{r}, \tag{5}$$

to be contrasted with the true magnetic moment

$$\mathbf{m} = \iiint_{\mathbb{R}^3} \mathbf{M}(\mathbf{r})\mathrm{d}^3\mathbf{r}. \tag{6}$$

Both quantities have dimensions of Am^2 and are expressed in Bohr magnetons $\mu_{\mathrm{B}} = 9.274\times10^{-24}\,\mathrm{J\,T}^{-1}$.

Using $\mathbf{B} = \nabla\times\mathbf{A}$ and the divergence theorem, Eq. (5) becomes

$$\begin{aligned}\mathbf{m}^{\mathrm{B}} &= \frac{1}{\mu_0}\iiint_{D\otimes\mathbb{R}} \nabla\times\mathbf{A}(\mathbf{r})\mathrm{d}^3\mathbf{r} = \frac{1}{\mu_0}\iint_{\partial(D\otimes\mathbb{R})} \mathrm{d}\mathbf{S}\times\mathbf{A}(\mathbf{r})\\ &= \frac{\phi_0}{\pi\mu_0}\oint_{\partial D} \varphi_M(\mathbf{r}_\perp)\,\mathrm{d}\ell.\end{aligned} \tag{7}$$

Thus for any closed-path ∂D, the circulation of the magnetic phase yields $\mathbf{m}^{\mathrm{B}}$. The relationship between $\mathbf{m}^{\mathrm{B}}$ and the true moment $\mathbf{m}$ generally depends on the choice of integration path.

With the inductive moment defined via closed-path phase integration, we now relate it to the true magnetic moment of the sample. A full derivation of the volume integration of the magnetic induction for a uniformly magnetized body is given in Supplementary Notes 1 and 2. Summarized here is the key result that connects the *true* magnetic moment $\mathbf{m}$ of the sample to the *inductive* moment $\mathbf{m}^{\mathrm{B}}$ inferred from electron-optical phase measurements.

Starting from the vector potential $\mathbf{A}$ for a magnetic dipole [28] and substituting it into the expression for the magnetic induction (Eq. (7)),

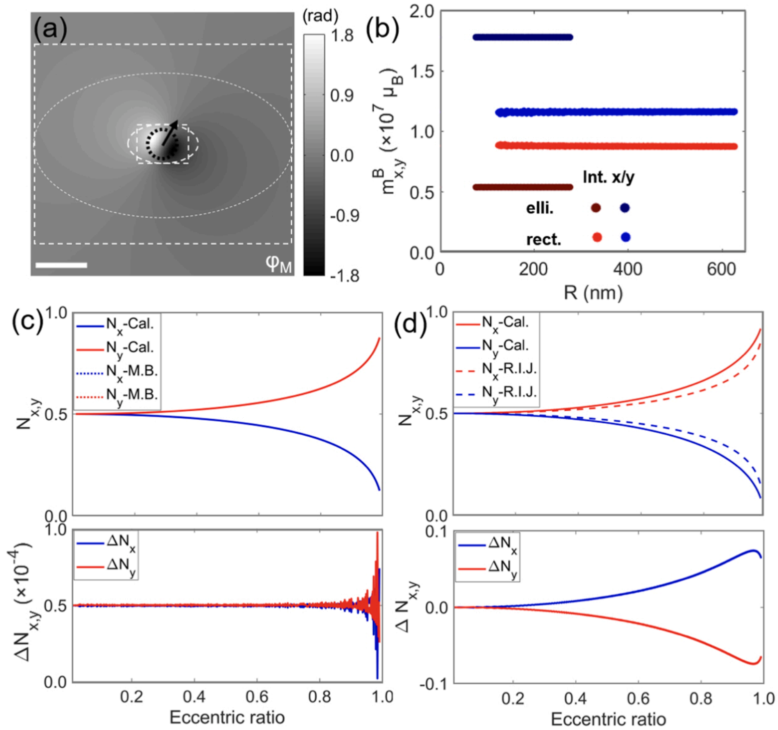

Fig. 2. Comparison of $N_{x,y}$ from phase integration and analytic formulas Comparison of demagnetization factors $N_{x,y}$ obtained from phase integration and analytic formulas. (a) simulated magnetic phase shift φ_M for a 50-nm-diameter sphere, showing integration paths. (b) inductive moments $m^{\mathrm{B}}_{x,y}$ obtained from closed-path phase integrals. (c,d) comparison of $N_{x,y}$ from phase integration for elliptical and rectangular paths with the analytic results from Beleggia *et al.* [29] (M.B.) and Joseph [30] (R.I.J.). Residuals show excellent agreement between the experimental results ($N_{x,y}$-Cal.) and the analytic formulas.

the field outside the sample can be expressed. However, in a practical inductive measurement, the detected flux links a path that encloses the sample. The general relationship between $\mathbf{m}^{\mathrm{B}}$ and $\mathbf{m}$ is given by

$$\mathbf{m}^{\mathrm{B}} = \mathbf{m} - \mathbf{m}_{\mathrm{H}}(D, \mathbf{M}), \tag{8}$$

where $\mathbf{m}_{\mathrm{H}}$ is a path-dependent term arising from demagnetizing fields. This term accounts for how the magnetic field lines are distorted by the sample's shape, with D representing the geometry of the integration path and $\mathbf{M}$ the magnetization, as shown in Supplementary Figure S1.

For a specific experimental geometry, this term can be expressed analytically. For a circular integration path of radius R, the demagnetizing factors of an infinite circular cylinder give the simple relation [21]

$$\mathbf{m}^{\mathrm{B}} = \left[\frac{1}{2}m_x,\ \frac{1}{2}m_y,\ m_z\right]. \tag{9}$$

For a circular integration path, the in-plane components $(x,\ y)$ of the inductive moment $\mathbf{m}^{\mathrm{B}}$ are half those of the true moment $\mathbf{m}$. Note that electron holography does not record m_z. For an elliptical path, the in-plane components are reduced by the planar demagnetization factors $N_{x,y}$ of an infinite elliptical cylinder [29], which generalizes the result in Eq. (8).

To test the theoretical relationship between $\mathbf{m}^{\mathrm{B}}$ and $\mathbf{m}$ derived above, we performed numerical simulations on uniformly magnetized spheres. We extend the methodology for measuring the volume-averaged inductive moment $\mathbf{m}^{\mathrm{B}}$ by moving beyond circular paths (Fig. 1(c, d)) to incorporate elliptical and rectangular integration paths. Fig. 2(a) shows the simulated magnetic phase shift φ_M for a uniformly magnetized sphere (50 nm diameter), with representative elliptical and rectangular integration paths overlaid at the minimum and maximum radii. Fig. 2(b) presents a key finding, namely, the measured components $m^{\mathrm{B}}_{x,y}$ plotted as a function of integration path radius for both an ellipse and a rectangle with a fixed eccentric ratio of 0.66. The standard eccentricity of an ellipse is given by $e = \sqrt{1 - \frac{b^2}{a^2}}$, with $a > b$ as the semi-axes. By direct analogy, we define a pseudo-eccentricity for a rectangle with length a and width b (where $a \geq b$) using the same formula. Notably, while the absolute values of $m^{\mathrm{B}}_{x,y}$ differ between the elliptical and rectangular paths, due to their distinct shapes altering the integrated phase, the value for each closed path remains constant across different radii. This radius-independence confirms the artifact-free nature of the simulated phase images, in contrast to the radial dependence typically observed in real experimental data discussed below.

Our method determines the demagnetization factor $N_{x,y}$ directly from integration of magnetic phase shifts using specific integration geometries. We begin with the measured inductive moment $m^{\mathrm{B}}_{x,y}$, which is related to the material's true moment $m_{x,y}$ by $m^{\mathrm{B}}_{x,y} = (1 - N_{x,y})\, m_{x,y}$. Here, the factor $(1 - N_{x,y})$ accounts for the internal demagnetizing field. By applying this relationship to the integrated magnetic phase, we extract $N_{x,y}$ for a given sample of known $m_{x,y}$. In this manner, the demagnetization factors are obtained solely from the phase integration method, circumventing the need for geometric approximations [27] or magnetometric measurements.

Figs. 2(c,d) present this analysis systematically, plotting the derived demagnetization factors $N_{x,y}$-Cal. over a broad range of elliptical and rectangular paths as a function of their eccentricity or aspect ratio. These data represent a key finding, demonstrating directly how the demagnetization tensor components evolve with the sample's geometry.

To rigorously test the validity of the relationship $m^{\mathrm{B}}_{x,y} = (1 - N_{x,y})\, m_{x,y}$ and the overall phase integration method, we performed independent calculations of the demagnetization factors $N_{x,y}$ for each elliptical and rectangular shape using established analytical and numerical techniques [30,31]. These explicitly calculated reference values are plotted alongside our phase-integration-derived results in Fig. 2(c,d). The lower panels quantitatively display the difference $\Delta N_{x,y}$ between the two sets of values. The strong agreement observed across the entire range of geometries, with minimal discrepancy in $\Delta N_{x,y}$, provides compelling evidence for the accuracy of our approach. This consistency not only validates the specific relationship between $m^{\mathrm{B}}_{x,y}$ and $m_{x,y}$ but also

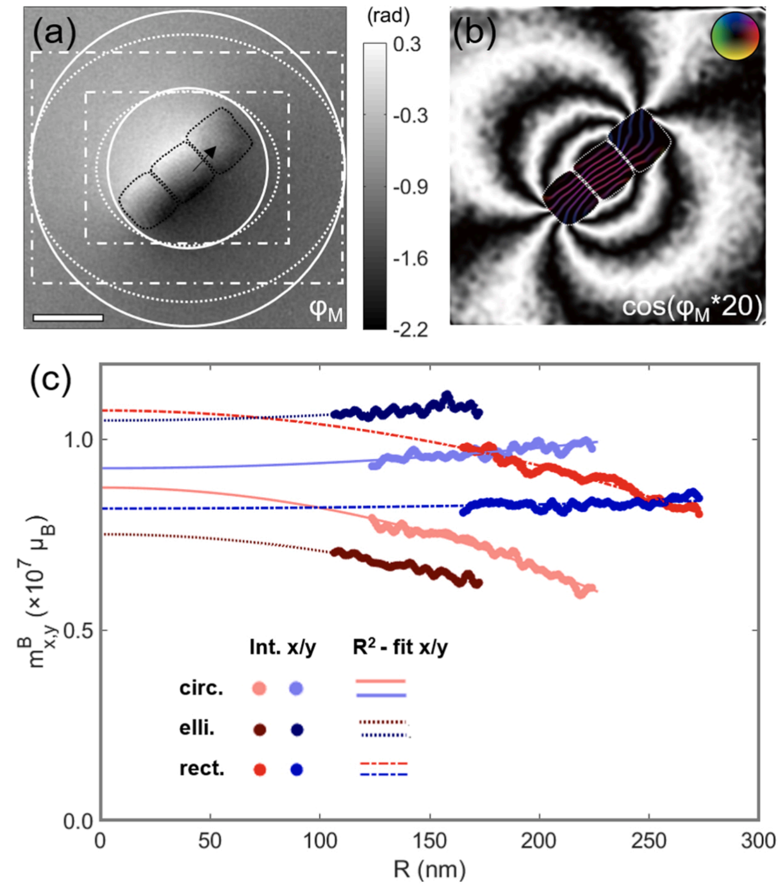

Fig. 3. Quantitative analysis of magnetic moments in Fe_3O_4 nanoparticles via phase integration Quantitative analysis of magnetic moments in Fe_3O_4 nanoparticles via phase integration. (a) experimental phase shift φ_M for three nanoparticles with integration paths (circular, elliptical, rectangular) at min/max radii. Scale bar: 200 nm. (b) projected in-plane magnetic induction via $\cos(20 \times \varphi_M)$, showing dipole-like stray fields. (c) inductive moments $m^{\mathrm{B}}_{x,y}$ extracted from phase integrations, demonstrating robustness across integration geometries.

underscores the general reliability and precision of the phase integration method for quantifying shape-dependent demagnetization fields in two-dimensional systems.

The experimental magnetic phase image φ_M of three Fe_3O_4 nanoparticles in Fig. 3(a) was acquired through a process that separates electric and magnetic contributions, as detailed in Supplementary Note 3. The resulting phase contours, presented as $\cos(20 \times \varphi_M)$ in Fig. 3(b), provide a two-dimensional projection of the in-plane component of the magnetic induction. For phase integration analysis, we defined three closed-path geometries on the phase image–a circle, an ellipse, and a rectangle–as indicated in Fig. 3(a). Quantitative analysis proceeded by integrating the phase shift along the x- and y-directions for each geometry over a range of integration radii. Fig. 3(c) shows the measured integrated phase shifts, their corresponding quadratic fits as a function of radius, and the extrapolated values in the zero-radius limit. From these extrapolated values, we determined the inductive magnetic moments. Using the known demagnetization factors appropriate for each closed-path geometry in Fig. 2(c,d), we then calculated the total magnetic moment of the three-particle ensemble; Table 1 summarizes the results. Additional experimental results on four Fe_3O_4 nanoparticles are reported in Supplementary Figure S3.

The magnetic moments obtained from the three integration geometries show excellent quantitative consistency, varying in magnitude by less than 0.5%. Minor angular deviations appeared, with the maximum discrepancy confined to 2.17°. This strong agreement validates the robustness of the phase integration method for determining total magnetic moments in nanomagnetic systems.

The close agreement among experimental results obtained from different integration geometries demonstrates the reliability of this approach. We now quantify its sensitivity to common experimental artifacts. Our previous report [21] showed that the error $\delta\mathbf{m}$ in the inductively measured magnetic moment $\mathbf{m}^{\mathrm{B}}$ scales quadratically with the radius R of the integration paths, i.e., $\delta\mathbf{m} \propto R^2$. These systematic errors stem from linear phase gradients, perturbations to the reference wave, and weak stray magnetic fields within the interferometric measurement [32–34]. To suppress these R^2-dependent contributions, we measure the inductive moment $\mathbf{m}^{\mathrm{B}}(R)$ for a series of integration paths with varying radii. We then fit a quadratic function to the data and take the value extrapolated to $R = 0$ as the corrected magnetic moment, which removes errors of $\delta\mathbf{m} \propto R^2$, as shown in Fig. 3(c).

We now extend the analysis to include two additional experimental factors that affect the accuracy of the phase integration method: Fresnel diffraction at the biprism filament and Gaussian noise in the acquired phase images [22,35]. Fig. 4(a) shows a simulated magnetic phase shift for a spherical particle under the combined influence of these effects. The simulation models Fresnel diffraction at a biprism voltage of 200 V, adds Gaussian noise to achieve a signal-to-noise ratio (SNR) of 22.74 dB, and incorporates the previously established quadratic scaling of phase errors. As detailed in Supplementary Note 4 and Figure S4-S6, the magnitudes of these perturbations—charging effects, noise, and diffraction—are derived from independent quantitative analyses, ensuring the simulated phase distribution replicates typical experimental conditions.

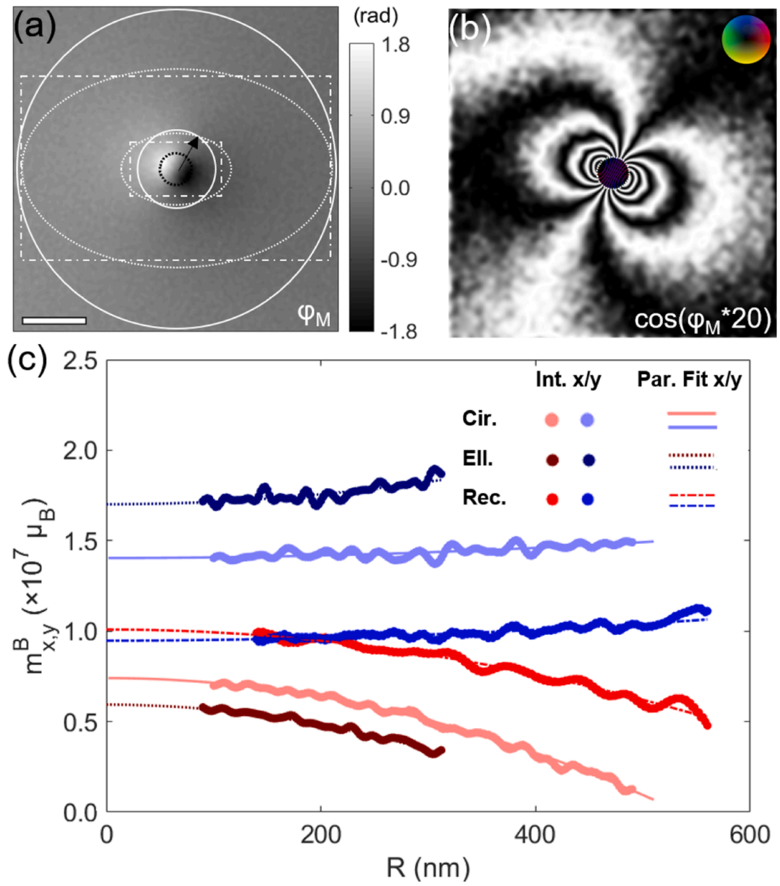

Fig. 4. Systematic analysis of error sources in magnetic moment quantification Systematic analysis of error sources in magnetic moment quantification. (a) Simulated phase image φ_M of a magnetic sphere with experimental perturbations (noise, Fresnel fringes, quadratic scaling errors). Integration paths (circular, elliptical, rectangular) shown at min/max radii. Scale bar: 100 nm. (b) Projected in-plane magnetic induction $\cos(20 \times \varphi_M)$, illustrating signal degradation from added artifacts. (c) Inductive moments $m^{\mathrm{B}}_{x,y}$ extracted from closed-path phase integrations. Deviation from ground truth quantifies systematic error from each perturbation.

For this simulated phase image, we applied the phase integration method using demagnetization factors determined previously for elliptical and rectangular closed-path geometries. The phase contour map in Fig. 4(b) represents the corresponding stray field distribution in projection. The close agreement between these derived stray fields and experimental observations confirms that the simulation captures the key phase perturbations present in practical measurements.

Fig. 4(c) plots the measured inductive signal as a function of integration radius for the three closed-path geometries, along with quadratic fits. For each geometry, we determined the magnetic moment **m** by extrapolating the fitted curve to zero radius and scaling by the geometry-specific demagnetization factor. Table 1 summarizes the results. Despite substantial variation in demagnetization factors across paths, the extracted magnetic moments—both in magnitude and orientation—agree excellently with the predefined simulation values. This consistency across independent geometric constraints validates the robustness of the phase integration method. The technique reliably quantifies magnetic moments under realistic phase perturbations, such as noise and Fresnel diffraction. Moreover, the availability of multiple distinct geometries enhances flexibility, allowing adaptation to diverse experimental conditions without compromising accuracy.

We have revisited the phase integration method for measuring magnetic moments by applying closed-path phase integration to simulated magnetic phases across three geometries: circular, elliptical, and rectangular. The results validate the theoretical framework for extracting demagnetization factors and establish a numerical approach for two-dimensional magnetic moment measurement. Both simulations and experiments confirm the method's accuracy and reliability.

A circular integration path offers two practical advantages. First, its rotational symmetry cancels contributions from higher-order multipoles–quadrupole, octupole, and beyond–leaving only the dipole moment. Second, the result does not depend on where the object sits within the path. The trade-off is that this symmetry discards information encoded in those higher-order terms: details about the object's position and any non-uniformity in its magnetization. Recovering that information requires breaking the symmetry with non-circular paths, such as squares or rectangles.

Beyond measuring moments, the method provides a practical route to estimating the two-dimensional area-averaged demagnetization factor. This capability supports more precise characterization of 2D magnetic materials [36] and thin films [37]. The current implementation measures only the projected in-plane component $m^{\mathrm{B}}_{x,y}$, but the full vector $\mathbf{m}^{\mathrm{B}}$ can be recovered through tilt-series reconstruction [38,39]. Together with the nanoscale spatial resolution inherent to transmission electron microscopy, these capabilities make phase-based TEM well suited for magnetic field imaging and moment measurement. As spatiotemporal resolution and phase sensitivity continue to improve, the technique is positioned to enable dynamic tracking of magnetic materials and real-time monitoring of their moments.

The approach applies equally to phase shifts obtained from other phase-contrast techniques [40,41], including in-line electron holography, differential phase contrast (DPC) imaging, and ptychography in scanning TEM. These methods offer complementary sensitivity for

Table 1
Experimental and simulation phase measurement results experimental and simulation phase measurement results.

	Eccentric ratio	m ($\times 10^7 \mu_B$)	m_θ (degree)	Error
Experimental				
Circle	0	2.5349	46.89	–
Ellipse	0.5064	2.5242	47.20	–
Rectangle	0.5462	2.5204	45.03	–
Simulation				
Simulation	–	3.1598	61.49	–
Circle	0	3.1686	62.25	0.28%, 0.76°
Ellipse	0.4401	3.1596	61.18	-0.01%, -0.31°
Rectangle	0.7806	3.1522	60.82	-0.24%, -0.67°

electric and magnetic field detection at the nanoscale, with established applications in charge [20] and moment [21] quantification.

We have derived a quantitative relationship between the inductive and true magnetic moments from the volume integral of the magnetic induction for a uniformly magnetized object. This expression allows the magnetic moment to be measured from the electron-optical phase shift in phase-based electron microscopy–an approach we validated through simulation and experiment. To assess its practical limits, we examined three closed-path geometries and considered key holographic artifacts: Gaussian noise, Fresnel diffraction, and charging effects. Simulations show the method is robust, with errors below 1% in moment magnitude and angular deviations under 1° under realistic conditions. Our results establish a framework for quantitative magnetic characterization in transmission electron microscopy, enabling precise analysis of nanoscale magnetic moments.

CRediT authorship contribution statement

Hangbo Su: Conceptualization, Formal analysis, Investigation, Methodology, Software, Validation, Visualization, Writing – original draft; **Xianhui Ye:** Formal analysis, Investigation, Validation, Writing – original draft; **Jiaqi Su:** Formal analysis, Investigation, Visualization, Writing – review & editing; **Yuying Liu:** Data curation, Investigation, Validation, Writing – review & editing; **Zian Li:** Data curation, Investigation, Validation, Writing – review & editing; **András Kovács:** Data curation, Investigation, Validation, Writing – review & editing; **Rafal E. Dunin-Borkowski:** Conceptualization, Methodology, Resources, Supervision, Writing – review & editing; **Marco Beleggia:** Conceptualization, Formal analysis, Methodology, Validation, Writing – review & editing.

Declaration of competing interest

The authors declare that they have no known competing financial interests or personal relationships that could have appeared to influence the work reported in this paper.

Acknowledgements

This work was supported by the National Natural Science Foundation of China (No. 12364018), Guangxi Science and Technology Major Program (No. AA23073019), and Natural Science Foundation of Guangxi Province (No. 2024GXNSFDA010014). The Center for Instrumental Analysis of Guangxi University is acknowledged for providing research facilities and resources for the experiments.

Data availability

The data that support the findings of this study are available within the article and its supplementary material. Additional data are available from the corresponding author upon reasonable request.

Supplementary material

Supplementary material associated with this article can be found in the online version at 10.1016/j.physleta.2026.132054.

References

[1] W.S. Huxter, M.F. Sarott, M. Trassin, C.L. Degen, Imaging ferroelectric domains with a single-spin scanning quantum sensor, Nat. Phys. 19 (5) (2023) 644–648. https://doi.org/10.1038/s41567-022-01921-4
[2] O.J. Amin, A. Dal Din, E. Golias, Y. Niu, A. Zakharov, S.C. Fromage, C.J.B. Fields, S.L. Heywood, R.B. Cousins, F. Maccherozzi, J. Krempaský, J.H. Dil, D. Kriegner, B. Király, R.P. Campion, A.W. Rushforth, K.W. Edmonds, S.S. Dhesi, L. Šmejkal, T. Jungwirth, P. Wadley, Nanoscale imaging and control of altermagnetism in MnTe, Nature 636 (8042) (2024) 348–353. https://doi.org/10.1038/s41586-024-08234-x
[3] J. Rovny, Z. Yuan, M. Fitzpatrick, A.I. Abdalla, L. Futamura, C. Fox, M.C. Cambria, S. Kolkowitz, N.P. de Leon, Nanoscale covariance magnetometry with diamond quantum sensors, Science 378 (6626) (2022) 1301–1305. https://doi.org/10.1126/science.ade9858
[4] M. Checa, A.S. Fuhr, C. Sun, R. Vasudevan, M. Ziatdinov, I. Ivanov, S.J. Yun, K. Xiao, A. Sehirlioglu, Y. Kim, Q. Wang, S.A. Morin, S.V. Kalinin, N. Balke, S. Jesse, P. Gentile, J.A. Brehm, R. Waser, D.J. Srolovitz, E. Zarkadoula, High-speed mapping of surface charge dynamics using sparse scanning Kelvin probe force microscopy, Nat. Commun. 14 (1) (2023) 7196. https://doi.org/10.1038/s41467-023-42583-x
[5] M. Bocarsly, M. Uzan, I. Roy, S. Grover, J. Xiao, Z. Dong, M. Labendik, A. Uri, M.E. Huber, Y. Myasoedov, K. Watanabe, T. Taniguchi, B. Yan, L.S. Levitov, E. Zeldov, De Haas–van Alphen spectroscopy and magnetic breakdown in moiré graphene, Science 383 (6678) (2024) 42–48. https://doi.org/10.1126/science.adh3499
[6] W. Niu, S. Sopp, A. Lodi, A. Gee, F. Kong, T. Pei, P. Gehring, J. Nägele, C.S. Lau, J. Ma, J. Liu, A. Narita, J. Mol, M. Burghard, K. Müllen, Y. Mai, X. Feng, L. Bogani, Exceptionally clean single-electron transistors from solutions of molecular graphene nanoribbons, Nat. Mater. 22 (2) (2023) 180–185. https://doi.org/10.1038/s41563-022-01460-6
[7] K. Shibata, M. Yoshida, K. Hirakawa, T. Otsuka, S.Z. Bisri, Y. Iwasa, Single PbS colloidal quantum dot transistors, Nat. Commun. 14 (1) (2023) 7486. https://doi.org/10.1038/s41467-023-43343-7
[8] Y.L. Huang, M. Song, C.-M. Lee, Y.-W. Chen, C.-Y. Chiang, S.-H. Chou, L.-C. Hsu, H.-J. Liu, G.-L. Chen, S.-Y. Yang, Y.-J. Chang, I.-J. Wang, Y.-C. Hsin, Y.-H. Su, J.-H. Wei, F. Xue, S.X. Wang, X. Bao, A 64-kilobit spin–orbit torque magnetic random-access memory based on back-end-of-line-compatible β-tungsten, Nat. Electron. 8 (9) (2025) 794–802. https://doi.org/10.1038/s41928-025-01434-x
[9] R. Gupta, C. Bouard, F. Kammerbauer, J.O. Ledesma-Martin, A. Bose, I. Kononenko, S. Martin, P. Usé, G. Jakob, M. Drouard, M. Kläui, Harnessing orbital Hall effect in spin-orbit torque MRAM, Nat. Commun. 16 (1) (2025) 130. https://doi.org/10.1038/s41467-024-55437-x
[10] T. Esat, D. Borodin, J. Oh, A.J. Heinrich, F.S. Tautz, Y. Bae, R. Temirov, A quantum sensor for atomic-scale electric and magnetic fields, Nat. Nanotechnol. 19 (10) (2024) 1466–1471. https://doi.org/10.1038/s41565-024-01724-z
[11] Z. Chen, E. Turgut, Y. Jiang, K.X. Nguyen, M.J. Stolt, S. Jin, D.C. Ralph, G.D. Fuchs, D.A. Muller, Lorentz electron ptychography for imaging magnetic textures beyond the diffraction limit, Nat. Nanotechnol. 17 (11) (2022) 1165–1170. https://doi.org/10.1038/s41565-022-01224-y
[12] J. Martis, S. Susarla, A. Rayabharam, C. Su, T. Paule, P. Pelz, C. Huff, X. Xu, H.-K. Li, M. Jaikissoon, V. Chen, E. Pop, K. Saraswat, A. Zettl, N.R. Aluru, R. Ramesh, P. Ercius, A. Majumdar, Imaging the electron charge density in monolayer MoS_2 at the {AAngstrom scale, Nat. Commun. 14 (1) (2023) 4363. https://doi.org/10.1038/s41467-023-39304-9
[13] D. Kong, A. Kovács, M. Charilaou, F. Zheng, L. Wang, X. Han, R.E. Dunin-Borkowski, Direct observation of tensile-strain-induced nanoscale magnetic hardening, Nat. Commun. 14 (1) (2023) 3963. https://doi.org/10.1038/s41467-023-39650-8
[14] S. Kang, M. Töllner, D. Wang, C. Minnert, K. Durst, A. Caron, R.E. Dunin-Borkowski, J. McCord, C. Kübel, X. Mu, Large-angle Lorentz four-dimensional scanning transmission electron microscopy for simultaneous local magnetization, strain and structure mapping, Nat. Commun. 16 (1) (2025) 1305. https://doi.org/10.1038/s41467-025-56521-6
[15] H. Lichte, M. Lehmann, Electron holography–basics and applications, Rep. Prog. Phys. 71 (1) (2008) 016102. https://doi.org/10.1088/0034-4885/71/1/016102
[16] Y. Aharonov, D. Bohm, Significance of electromagnetic potentials in the quantum theory, Phys. Rev. 115 (3) (1959) 485. https://doi.org/10.1103/PhysRev.115.485
[17] M.R. McCartney, N. Agarwal, S. Chung, D.a. Cullen, M.-G. Han, K. He, L. Li, H. Wang, L. Zhou, D.J. Smith, Quantitative phase imaging of nanoscale electrostatic and magnetic fields using off-axis electron holography, Ultramicroscopy 110 (2010) 375–382. https://doi.org/10.1016/j.ultramic.2010.01.001
[18] D. Shindo, T. Tanigaki, H.S. Park, Advanced electron holography applied to electromagnetic field study in materials science, Adv. Mater. 29 (2017) 1602216. https://doi.org/10.1002/adma.201602216
[19] M. Beleggia, T. Kasama, R.E. Dunin-Borkowski, S. Hofmann, G. Pozzi, Direct measurement of the charge distribution along a biased carbon nanotube bundle using electron holography, Appl. Phys. Lett. 98 (24) (2011). https://doi.org/10.1063/1.3598468
[20] C. Gatel, A. Lubk, G. Pozzi, E. Snoeck, M. Hÿtch, Counting elementary charges on nanoparticles by electron holography, Phys. Rev. Lett. 111 (2) (2013) 025501. https://doi.org/10.1103/PhysRevLett.111.025501

[21] M. Beleggia, T. Kasama, R.E. Dunin-Borkowski, The quantitative measurement of magnetic moments from phase images of nanoparticles and nanostructures–I. fundamentals, Ultramicroscopy 110 (5) (2010) 425–432. https://doi.org/10.1016/j.ultramic.2009.10.007

[22] J. Caron, Model-Based Reconstruction of Magnetisation Distributions in Nanostructures from Electron Optical Phase Images, Ph.d. dissertation, RWTH Aachen University, Aachen, Germany, 2017. Dissertation, RWTH Aachen University, 2017.

[23] T. Tanigaki, T. Akashi, T. Yoshida, K. Harada, K. Ishizuka, M. Ichimura, K. Mitsuishi, Y. Tomioka, X. Yu, D. Shindo, Y. Tokura, Y. Murakami, H. Shinada, Electron holography observation of individual ferrimagnetic lattice planes, Nature 631 (8021) (2024) 521–525. https://doi.org/10.1038/s41586-024-07673-w

[24] F. Zheng, N.S. Kiselev, F.N. Rybakov, L. Yang, W. Shi, S. Blügel, R.E. Dunin-Borkowski, Hopfion rings in a cubic chiral magnet, Nature 623 (7988) (2023) 718–723. https://doi.org/10.1038/s41586-023-06658-5

[25] X. Ye, H. Su, J. Su, A. Kovács, M. Beleggia, R.E. Dunin-Borkowski, Z.-A. Li, Quantification of magnetization of nanostructures via three complementary methods, Appl. Phys. Lett. 126 (24) (2025). https://doi.org/10.1063/5.0266886

[26] A. Kovács, M. Pósfai, B. Zingsem, Z.-A. Li, P. Pekker, J. Caron, S. Prévéral, C.T. Lefèvre, D.A. Bazylinski, R.B. Frankel, R.E. Dunin-Borkowski, Influence of crystal shape and orientation on the magnetic microstructure of bullet-shaped magnetosomes synthesized by magnetotactic bacteria, Geo-Bio Interfaces 1 (2024) e1. https://doi.org/10.1180/gbi.2024.3

[27] R. Moskowitz, E. Della Torre, Theoretical aspects of demagnetization tensors, IEEE Trans. Magn. 2 (4) (1966) 739–744. https://doi.org/10.1109/TMAG.1966.1065973

[28] J.D. Jackson, Classical Electrodynamics, John Wiley & Sons, 3 ed., 1998.

[29] M. Beleggia, M. De Graef, Y.T. Millev, D.A. Goode, G. Rowlands, Demagnetization factors for elliptic cylinders, J. Phys. D Appl. Phys. 38 (18) (2005) 3333. https://doi.org/10.1088/0022-3727/38/18/001

[30] R.I. Joseph, E. Schlomann, Demagnetizing field in nonellipsoidal bodies, J. Appl. Phys. 36 (5) (1965) 1579–1593. https://doi.org/10.1063/1.1703091

[31] H. Fukushima, Y. Nakatani, N. Hayashi, Volume average demagnetizing tensor of rectangular prisms, IEEE Trans. Magn. 34 (1) (1998) 193–198. https://doi.org/10.1109/20.650225

[32] F. Roder, A. Lubk, D. Wolf, T. Niermann, Noise estimation for off-axis electron holography, Ultramicroscopy 144 (2014) 32–42. https://doi.org/10.1016/j.ultramic.2014.04.002

[33] T. Wagner, R. Kraft, F. Nowak, D. Berger, C.M. Günther, H. Çelik, C.T. Koch, M. Lehmann, The reference window for reduced perturbation of the reference wave in electrical biasing off-axis electron holography, Ultramicroscopy 267 (2024) 114060. https://doi.org/10.1016/j.ultramic.2024.114060

[34] G. Matteucci, M. Muccini, U. Hartmann, Electron holography in the study of the leakage field of magnetic force microscope sensor tips, Appl. Phys. Lett. 62 (15) (1993) 1839. https://doi.org/10.1063/1.109566

[35] K. Yamamoto, T. Tanji, M. Hibino, Hologram simulation for off-axis electron holography, Ultramicroscopy 85 (1) (2000) 35–49. https://doi.org/10.1016/S0304-3991(00)00042-5

[36] H.T. Diep, Physics of 2D magnets and magnetic thin films: surface structure and phase transitions, criticality and skyrmions, in: J.-C.S. Levy (Ed.), 2D and 3D Nanostructures: Structures, Properties, and Applications, Jenny Stanford Publishing, Singapore, 1 ed., 2026, p. 35.

[37] D.L. Cortie, G.L. Causer, K.C. Rule, H. Fritzsche, W. Kreuzpaintner, F. Klose, Two-dimensional magnets: forgotten history and recent progress towards spintronic applications, Adv. Funct. Mater. 30 (18) (2020) 1901414. https://doi.org/10.1002/adfm.201901414

[38] D. Wolf, N. Biziere, S. Sturm, D. Reyes, T. Wade, T. Niermann, J. Krehl, B. Warot-Fonrose, B. Büchner, E. Snoeck, C. Gatel, A. Lubk, Holographic vector field electron tomography of three-dimensional nanomagnets, Commun. Phys. 2 (1) (2019) 87. https://doi.org/10.1038/s42005-019-0187-8

[39] F.S. Yasin, J. Masell, Y. Takahashi, T. Akashi, N. Baba, K. Karube, D. Shindo, T. Arima, Y. Taguchi, Y. Tokura, T. Tanigaki, X. Yu, Bloch point quadrupole constituting hybrid topological strings revealed with electron holographic vector field tomography, Adv. Mater. 36 (16) (2024) 2311737. https://doi.org/10.1002/adma.202311737

[40] R. Streubel, Phase contrast imaging of non-collinear spin textures with Lorentz microscopy, J. Mater. Res. 38 (23) (2023) 4977–4994. https://doi.org/10.1557/s43578-023-01216-1

[41] G. Sanchez-Santolino, L. Clark, S. Toyama, T. Seki, N. Shibata, Phase imaging methods in the scanning transmission electron microscope, Nano Lett. 25 (27) (2025) 10709–10721. https://doi.org/10.1021/acs.nanolett.4c06697